Supporting Information

Rapid, self-sacrificing template synthesis of two dimension high-entropy oxides toward high-performance oxygen evolution

Xiaofeng Tian[a], Hongdong Li[a], Rui Chang[a], Yu Yang[a], Zhenhui Wang[a], Tian Dong[a], Jianping Lai[a], Shouhua Feng[a] and Lei Wang[a,b*]*

[a] Key Laboratory of Eco-Chemical Engineering, International Science and Technology Cooperation Base of Eco-Chemical Engineering and Green Manufacturing, College of Chemistry and Molecular Engineering, Qingdao University of Science and Technology, Qingdao 266042, P. R. China

[b] Shandong Engineering Research Center for Marine Environment Corrosion and Safety Protection, College of Environment and Safety Engineering, Qingdao University of Science and Technology, Qingdao 266042, P. R. China

E-mail: lihd@qust.edu.cn; inorchemwl@126.com

Experimental Section

Chemicals: $Fe(NO_3)_3 \cdot 9H_2O$, Ni $(NO_3)_2 \cdot 6H_2O$, $Cr(NO_3)_3 \cdot 9H_2O$, $RuCl_3$ were obtained from Aladdin. $Co(NO_3)_3 \cdot 6H_2O$ was procured from Macklin. $Mn(NO_3)_2 \cdot 4H_2O$, $Mo(CO)_6$ were purchased from Sigma-Aldrich. Potassium hydroxide (KOH, 90%) was bought from Aladdin. Nafion solution (5%) was acquired from Sigma-Aldrich. The deionized water in the experiment is ultrapure water (18.2 MΩ·cm).

Synthesis of high-entropy oxides: $Fe(NO_3)_3 \cdot 9H_2O$ (0.41 g), $Co(NO_3)_3 \cdot 6H_2O$ (0.29 g), $Ni(NO_3)_2 \cdot 6H_2O$ (0.30 g), $Mo(CO)_6$ (0.26 g), $RuCl_3$ (0.21 g) (0.1 mmol each) was poured into a mortar and ground evenly, then add 1 g cellulose powder and grind again until completely mixed, thus obtaining the precursor. The obtained precursor powder was placed in a container and heated in a Joule heating device at 150 A for 60 seconds and then 240 A for 60 seconds, and cooled and taken out after the reaction was finished. Similarly, $(FeCoNiCrMn)_3O_4$, $(FeCoNiMoMn)_3O_4$, $(FeCoNiMn)_3O_4$ and $(FeCoNi)_3O_4$ are synthesized, except that the type of metal salt is changed. (Replace metal salts with $Cr(NO_3)_3 \cdot 9H_2O$, $Mn(NO_3)_2 \cdot 4H_2O$ and $Mo(CO)_6$).

Materials characterization: The morphologies of materials were characterized by scanning electron microscope (SEM, Hitachi Regulus 8100), transmission electron microcopy (TEM) and high resolution TEM (HRTEM) (JEM-2100UHR at an accelerating voltage of 200 KV). Powder X-ray diffraction (XRD) spectra were recorded on an X'Pert-Pro MPD diffractometer (Netherlands PANalytical) operating at 40 KV and 40 mA with Cu Kα radiation. X-ray photoelectron spectrum (XPS) was conducted using VG ESCALABMK II spectrometer with Al Kα photon source.

Electrochemical FT-IR reflection spectroscopy was investigated on a Fourier transform infrared spectrometer (Thermo iS50 FT-IR).

Electrochemical measurements: The different catalysts were dispersed in isopropanol + ultrapure water + Nafion (v:v:v = 3:1:0.04) and sonicated for 30 min yielding highly dispersed suspensions with a concentration of 10 mg mL^{-1}. Then, 25 μL of the catalyst ink was dropped onto a clean carbon paper substrate. After drying at room temperature, the catalyst was loaded with approximately 0.50 mg cm^{-2}. Electrochemical measurements were conducted on a CHI 760 electrochemical workstation (Shanghai Chenhua Instrument Co., Ltd.). The electrochemical tests were carried out in a conventional three-electrode cell, Carbon paper was used as the working electrode, the graphite rod electrode as the counter electrode and a saturated calomel electrode (SCE) as the reference electrode. The potentials were calibrated to RHE: E (RHE) = E (SCE) + 0.241 V + 0.0592 × pH. All tests were compensated with 95% ohmic potential drop (IR). OER measurements were performed in 1 M KOH solution. The stability of samples was performed through 20000 CV cycles and chronoamperometry (i-t curve) test. Electrochemical impedance spectroscopy (EIS) measurements were measured at 1.55 V vs. RHE in the frequency range from 100 kHz to 0.1 Hz in 1.0 M KOH solution.

The TOF values were calculated by the following equation. Where, j is the current density, A is the geometric area of the working electrode, F is the Faraday constant and N is the number of active sites.

$$\mathrm{TOF} = \frac{jA}{2FN}$$

Here, the electrochemically active surface area (ECSA) of the catalysts is evaluated using the electrochemical double layer capacitance (Cdl) method. From the equation

Cs is the specific capacitance. Note that herein the general specific capacitance (Cs) in alkaline solution is around 0.04 mF cm^{-2}.

$$\text{ECSA} = \frac{Cdl}{Cs}$$

ρ^{RHE} reflects the dependence of OER reaction kinetics on proton activity, and the formula is as follows:

$$\rho^{RHE} = \frac{\partial \log (j)}{\partial \text{pH}}$$

Where pH ranges from 12.5 to 14 and log (j) is the logarithm of the current density at 1.5 V versus the RHE. The OER kinetics are almost independent of the solution pH. While proton-coupled electron transfer reactions are occurring, the OER kinetics is almost independent of the solution pH, resulting in a low ρ^{RHE}. If the OER involves non-co-operative proton-electron transfer, the OER kinetics will be strongly dependent on pH and have a large ρ^{RHE} value.

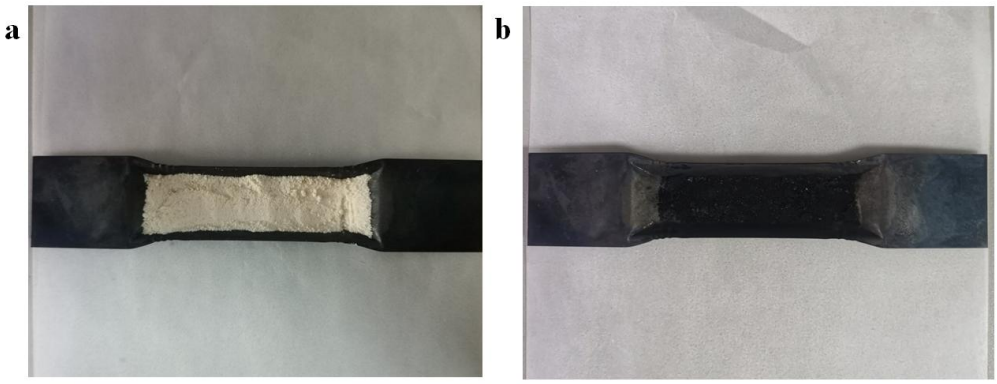

Figure S1. (a) Photographs of precursor, (b) Photographs of the synthesized high-entropy oxide via Joule-heating.

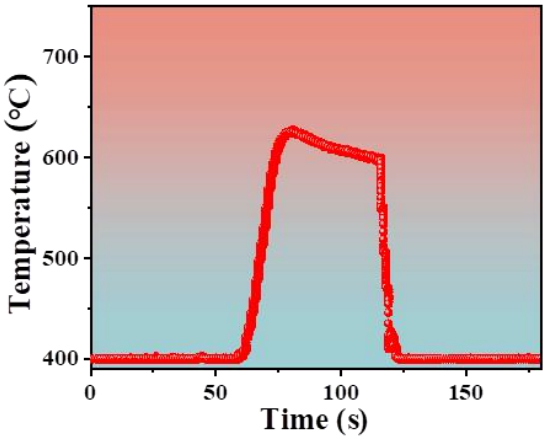

Figure S2. Time-temperature evolution during sample preparation.

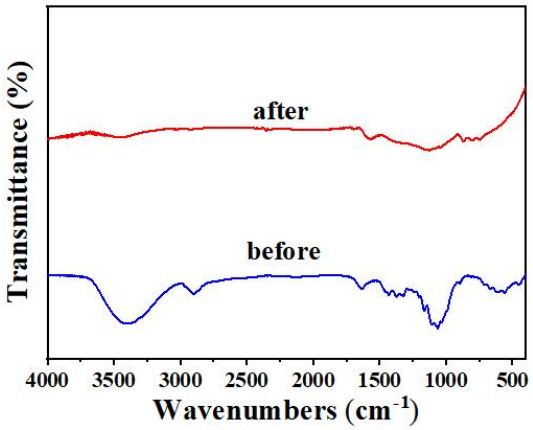

Figure S3. Comparison of FT-IR spectra of $(FeCoNiMoRu)_3O_4$ before and after Joule heating.

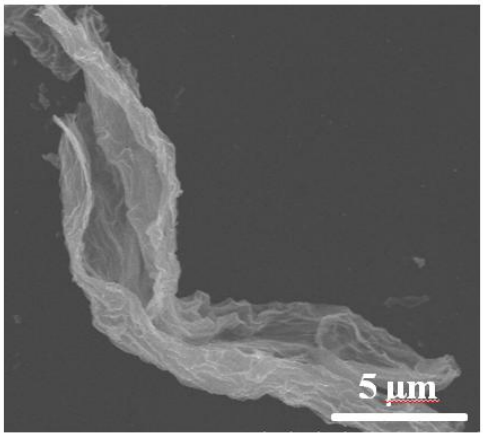

Figure S4. SEM image of $(FeCoNiMoRu)_3O_4$.

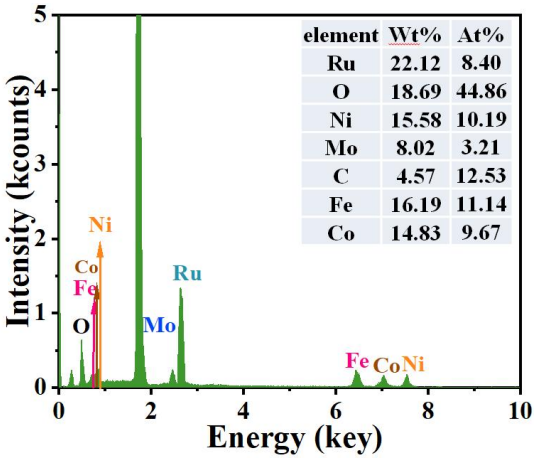

Figure S5. TEM-EDS of $(FeCoNiMoRu)_3O_4$.

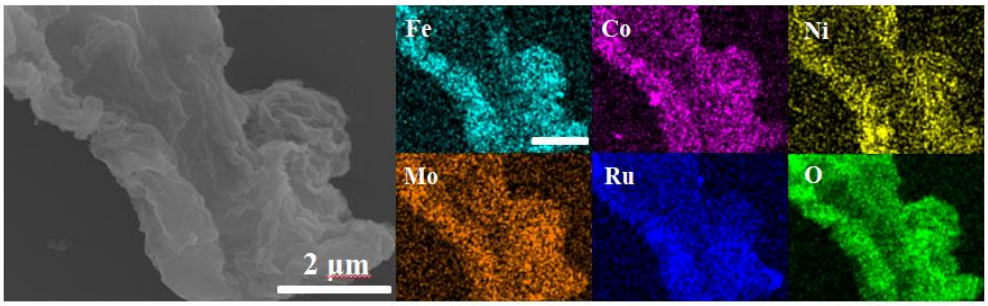

Figure S6. SEM-EDS mapping of $(FeCoNiMoRu)_3O_4$.

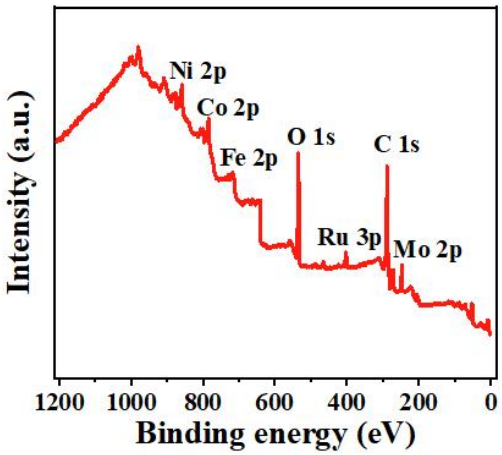

Figure S7. The XPS spectra of $(FeCoNiMoRu)_3O_4$.

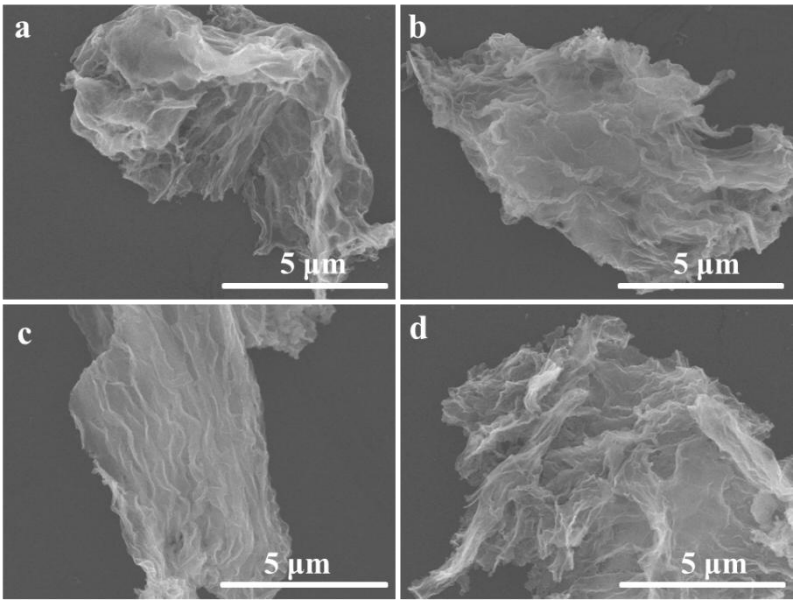

Figure S8. SEM images of (a) $(FeCoNiCrMn)_3O_4$, (b) $(FeCoNiMoMn)_3O_4$, (c) $(FeCoNiMn)_3O_4$ and (d) $(FeCoNi)_3O_4$.

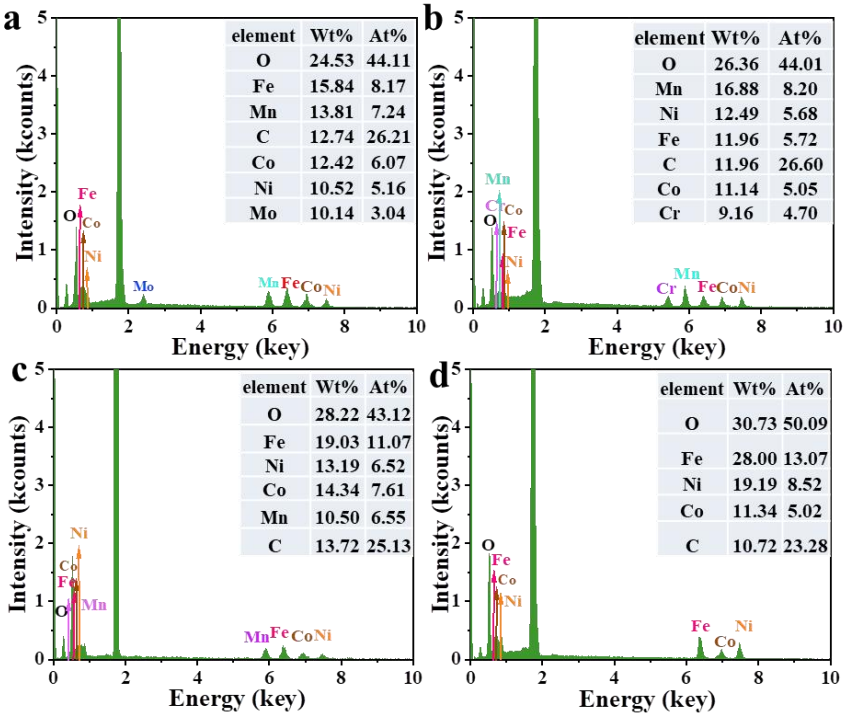

Figure S9. SEM-EDS spectra of (a) $(FeCoNiMoMn)_3O_4$, (b) $(FeCoNiCrMn)_3O_4$, (c) $(FeCoNiMn)_3O_4$ and (d) $(FeCoNi)_3O_4$.

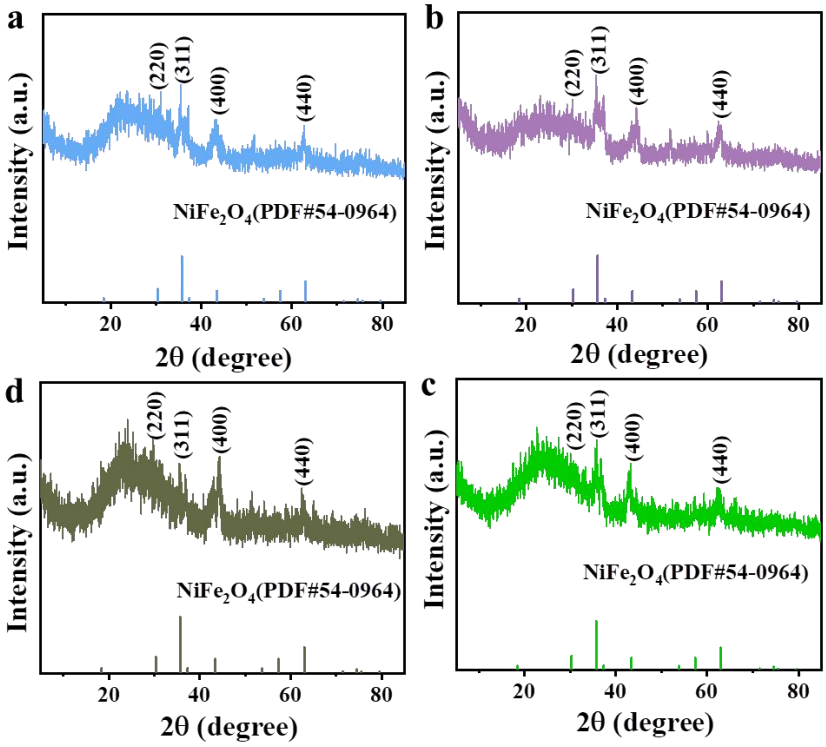

Figure S10. XRD patterns of (a) $(FeCoNiCrMn)_3O_4$, (b) $(FeCoNiMoMn)_3O_4$, (c) $(FeCoNiMn)_3O_4$ and (d) $(FeCoNi)_3O_4$.

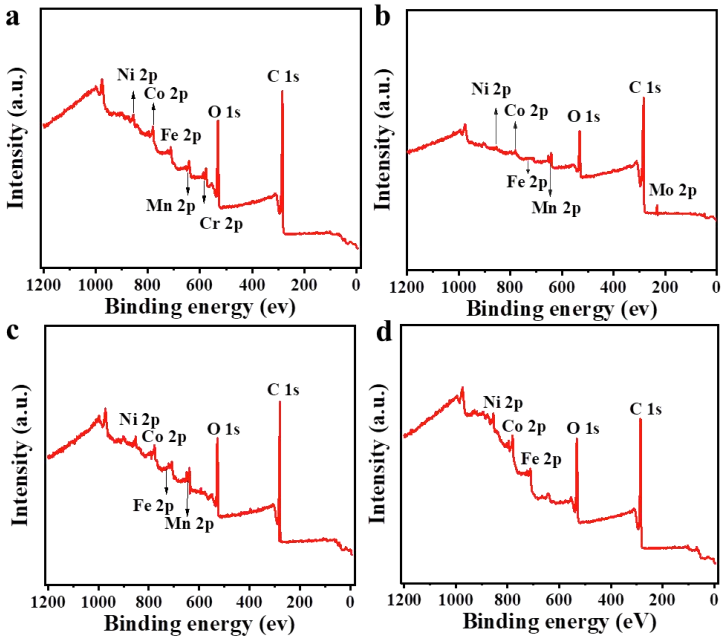

Figure S11. The XPS spectra of (a) $(FeCoNiCrMn)_3O_4$, (b) $(FeCoNiMoMn)_3O_4$, (c) $(FeCoNiMn)_3O_4$ and (d) $(FeCoNi)_3O_4$.

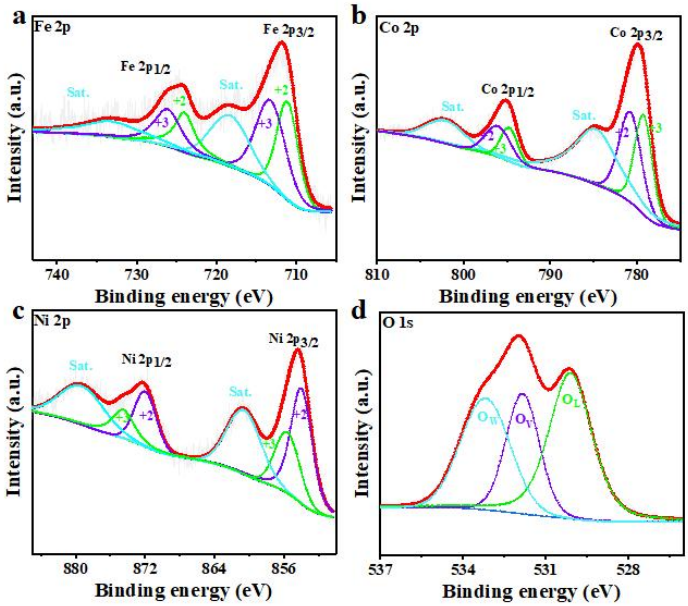

Figure S12. High resolution XPS spectra of (a) Fe 2p, (b) Co 2p, (c) Ni 2p, (d) O 1 s in $(FeCoNi)_3O_4$.

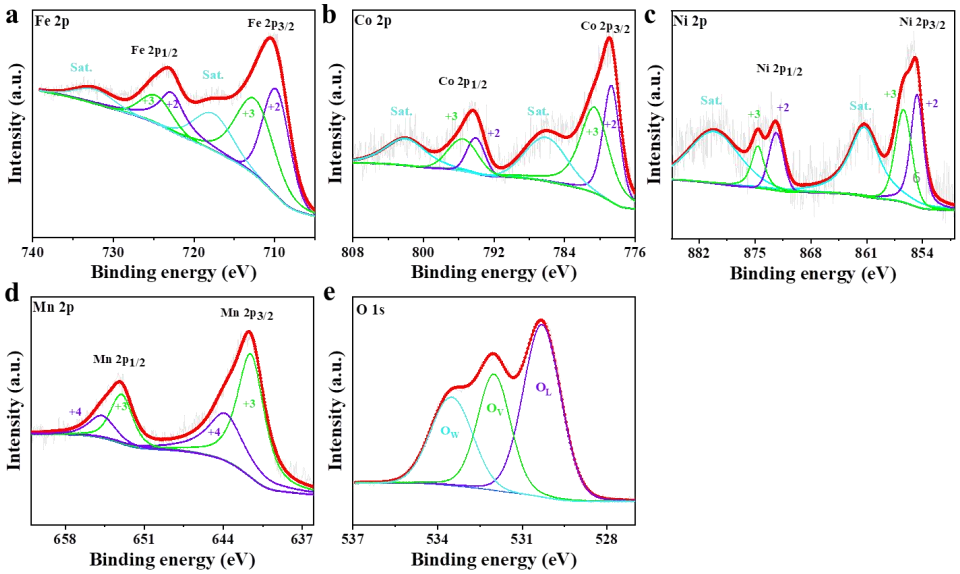

Figure S13. High resolution XPS spectra of (a) Fe 2p, (b) Co 2p, (c) Ni 2p, (d) Mn 2p, (e) O 1 s in $(FeCoNiMn)_3O_4$.

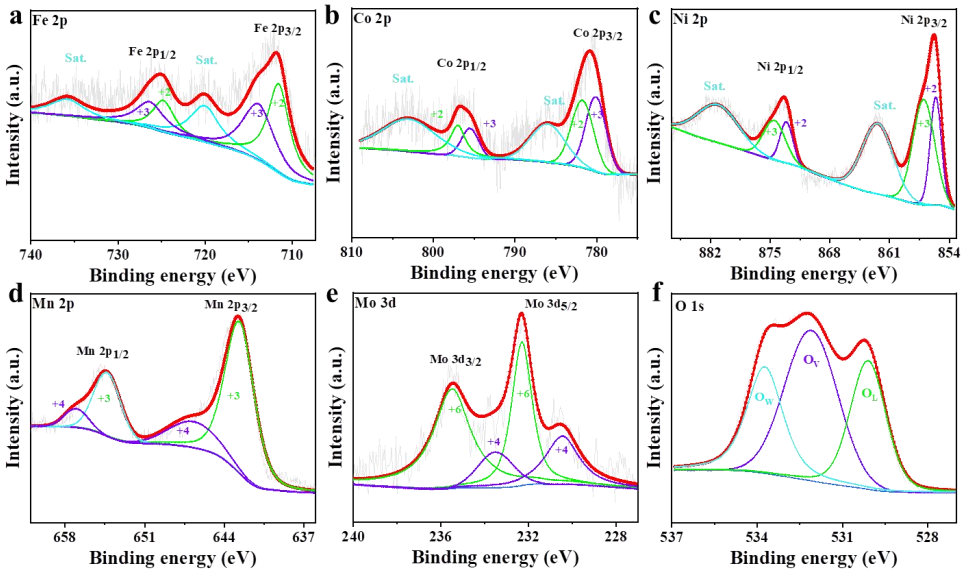

Figure S14. High resolution XPS spectra of (a) Fe 2p, (b) Co 2p, (c) Ni 2p, (d) Mn 2p, (e) Mo 3d, (f) O 1 s in $(FeCoNiMoMn)_3O_4$.

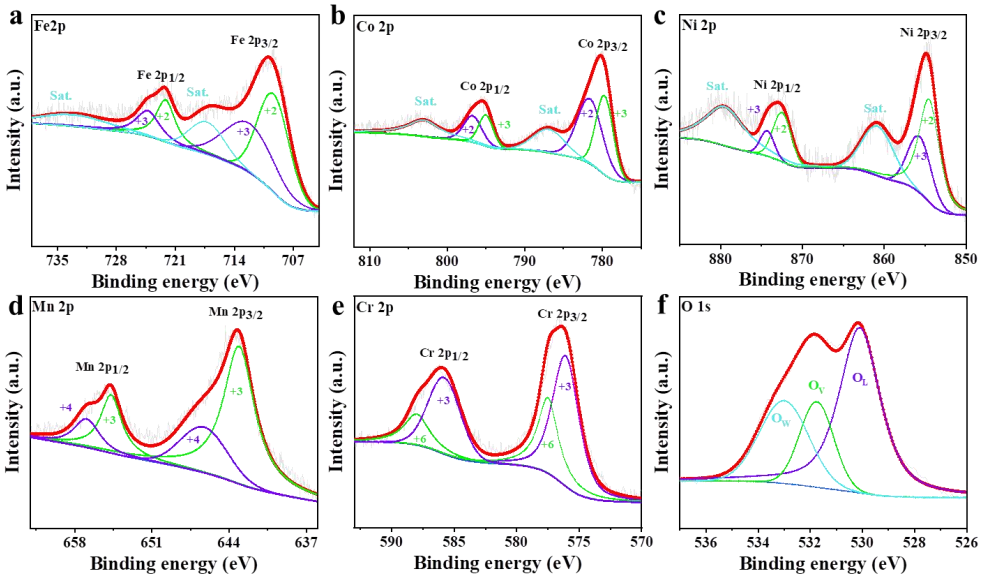

Figure S15. High resolution XPS spectra of (a) Fe 2p, (b) Co 2p, (c) Ni 2p, (d) Mn 2p, (e) Cr 2p, (f) O 1 s in $(FeCoNiCrMn)_3O_4$.

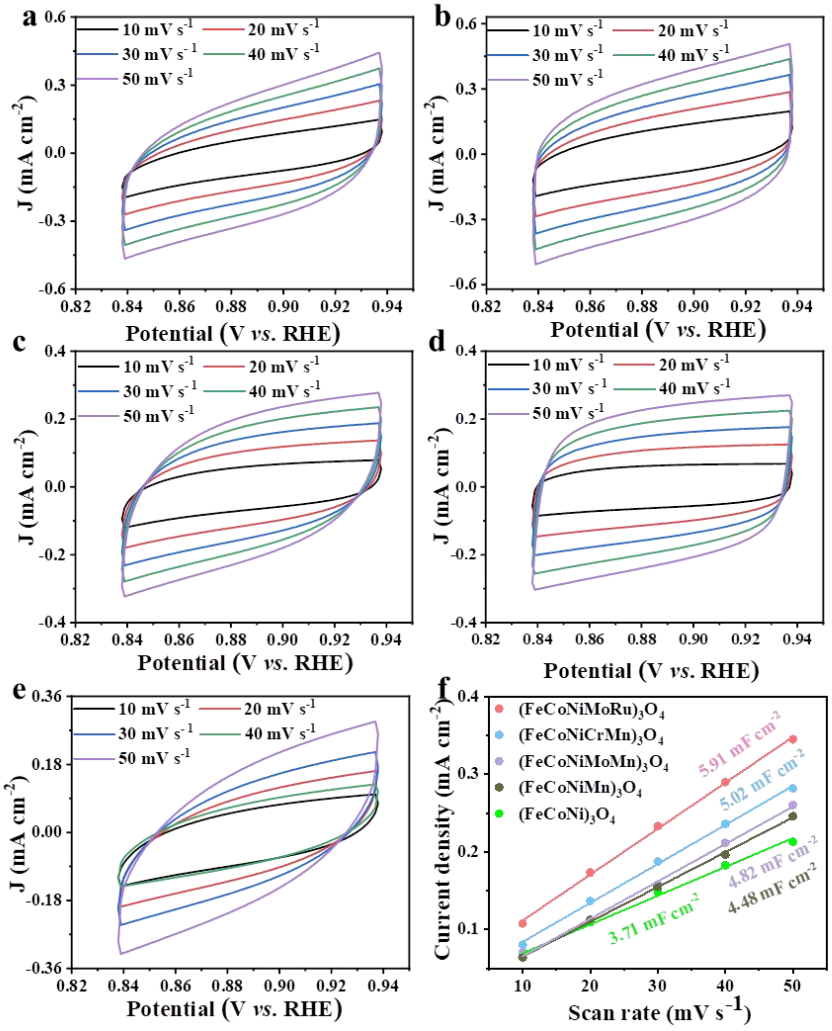

Figure S16. CV curves of (a) $(FeCoNiMoRu)_3O_4$, (b) $(FeCoNiCrMn)_3O_4$, (c) $(FeCoNiMoMn)_3O_4$, (d) $(FeCoNiMn)_3O_4$, and (e) $(FeCoNi)_3O_4$, (f) Estimation of Cdl by plotting the capacitive current density against the scan rate to fit a linear regression.

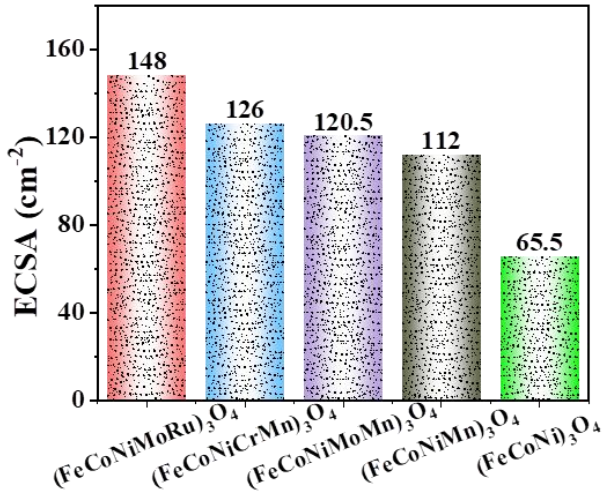

Figure S17. ECSA of $(FeCoNiMoRu)_3O_4$, $(FeCoNiCrMn)_3O_4$, $(FeCoNiMoMn)_3O_4$, $(FeCoNiMn)_3O_4$, and $(FeCoNi)_3O_4$.

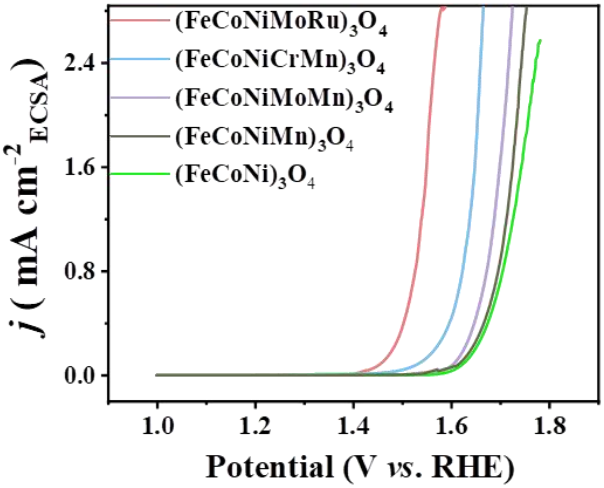

Figure S18. ECSA of $(FeCoNiMoRu)_3O_4$, $(FeCoNiCrMn)_3O_4$, $(FeCoNiMoMn)_3O_4$, $(FeCoNiMn)_3O_4$, and $(FeCoNi)_3O_4$.

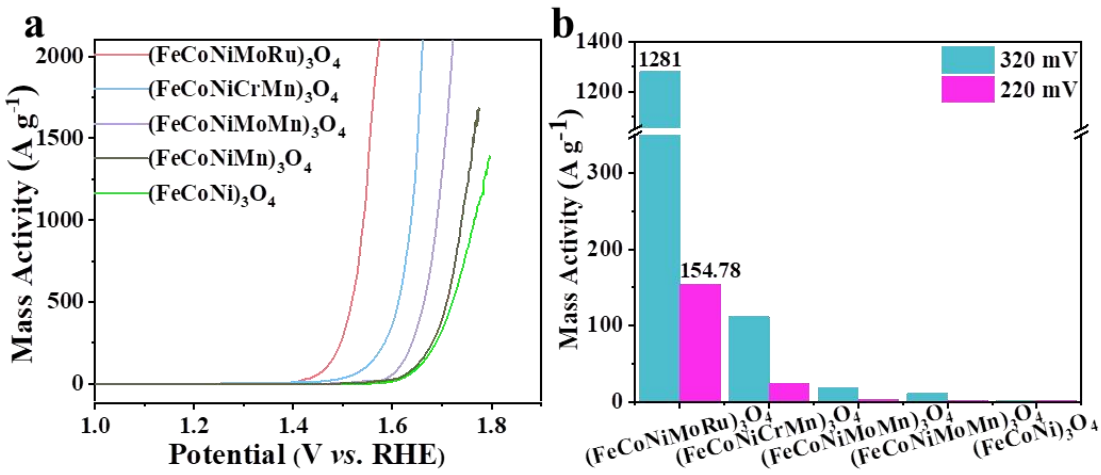

Figure S19. (a) Mass activity curves of $(FeCoNiMoRu)_3O_4$, $(FeCoNiCrMn)_3O_4$ $(FeCoNiMoMn)_3O_4$, $(FeCoNiMn)_3O_4$ and $(FeCoNi)_3O_4$ for OER. (b) Mass activity of $(FeCoNiMoRu)_3O_4$, $(FeCoNiCrMn)_3O_4$ $(FeCoNiMoMn)_3O_4$, $(FeCoNiMn)_3O_4$ and $(FeCoNi)_3O_4$ at the overpotential of 320 mV and 220 mV. All the five metals are considered.

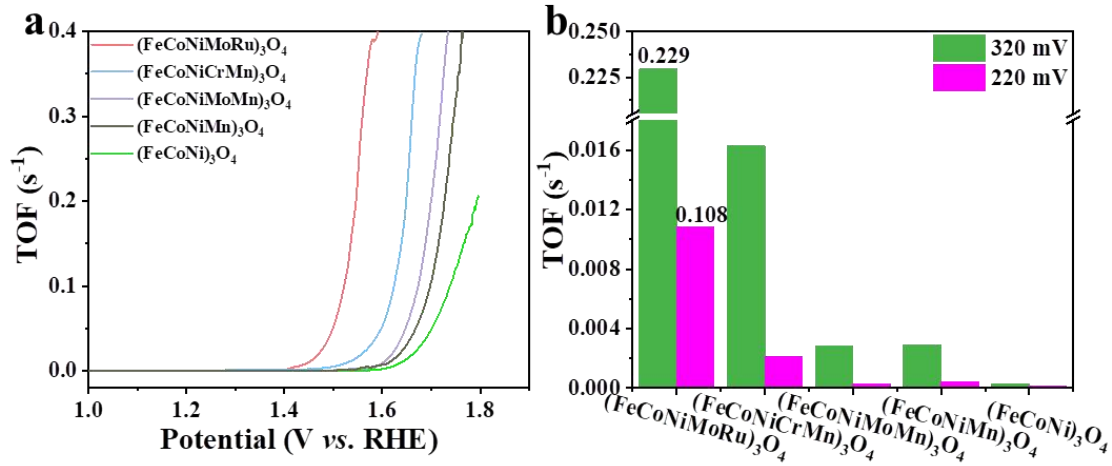

Figure S20. (a) The TOF values of $(FeCoNiMoRu)_3O_4$, $(FeCoNiCrMn)_3O_4$ $(FeCoNiMoMn)_3O_4$, $(FeCoNiMn)_3O_4$ and $(FeCoNi)_3O_4$ for OER. (b) TOF values of $(FeCoNiMoRu)_3O_4$, $(FeCoNiCrMn)_3O_4$ $(FeCoNiMoMn)_3O_4$, $(FeCoNiMn)_3O_4$ and $(FeCoNi)_3O_4$ at the overpotential of 320 mV and 220 mV. All the five metals are considered.

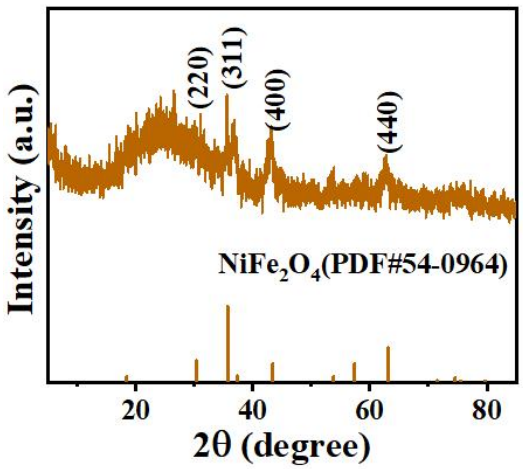

Figure S21. XRD pattern of $(FeCoNiMoRu)_3O_4$ after OER testing.

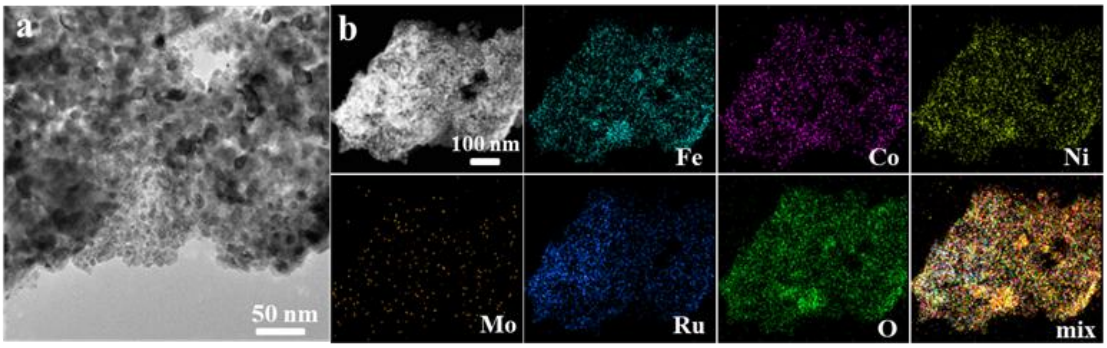

Figure S22. TEM image and TEM-EDS mapping of $(FeCoNiMoRu)_3O_4$ after OER testing.

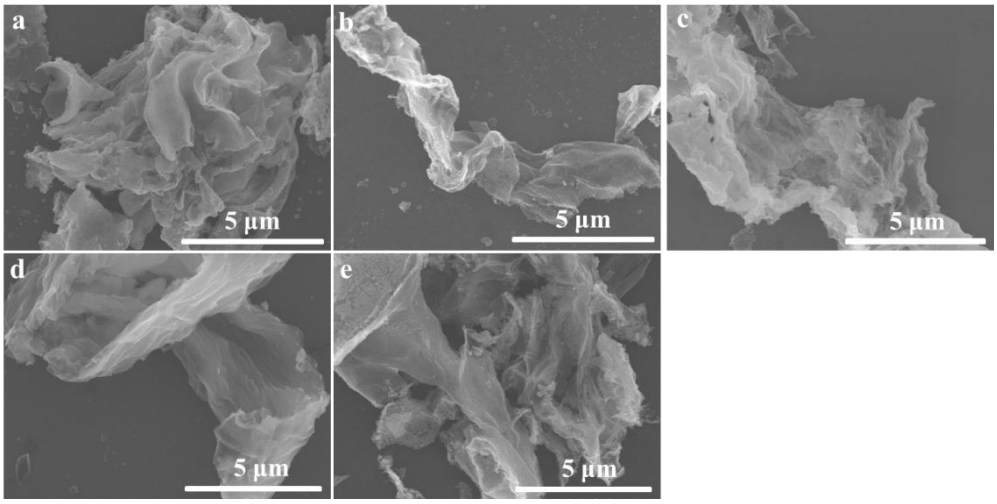

Figure S23. SEM images after OER testing. (a) $(FeCoNiMoRu)_3O_4$, (b) $(FeCoNiCrMn)_3O_4$, (c) $(FeCoNiMoMn)_3O_4$, (d) $(FeCoNiMn)_3O_4$ and (e) $(FeCoNi)_3O_4$.

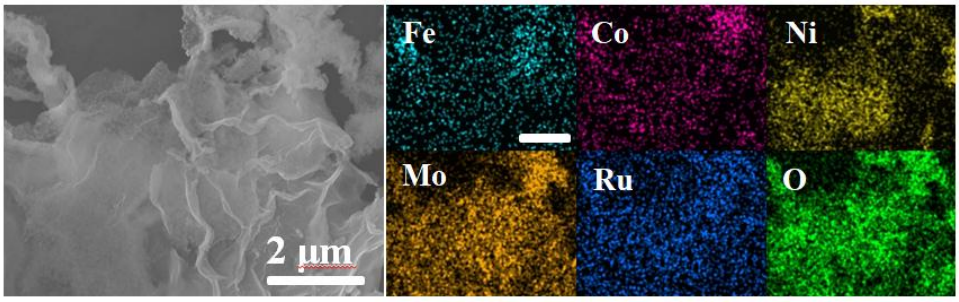

Figure S24. SEM-EDS mapping of $(FeCoNiMoRu)_3O_4$ after OER testing.

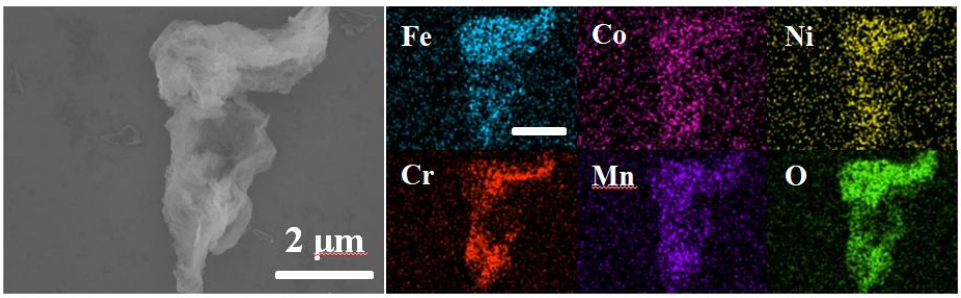

Figure S25. SEM-EDS mapping of $(FeCoNiCrMn)_3O_4$ after OER testing.

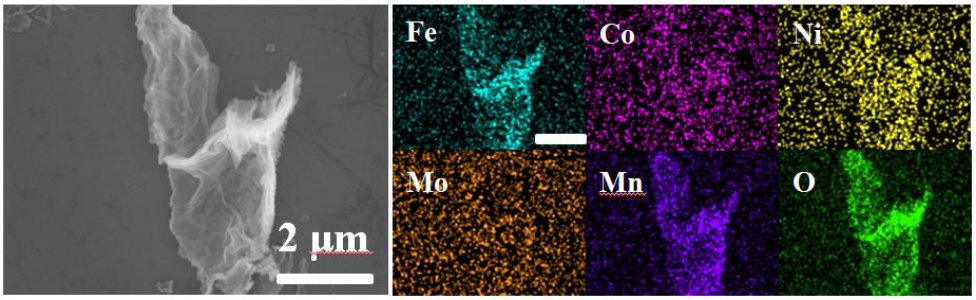

Figure S26. SEM-EDS mapping of $(FeCoNiMoMn)_3O_4$ after OER testing.

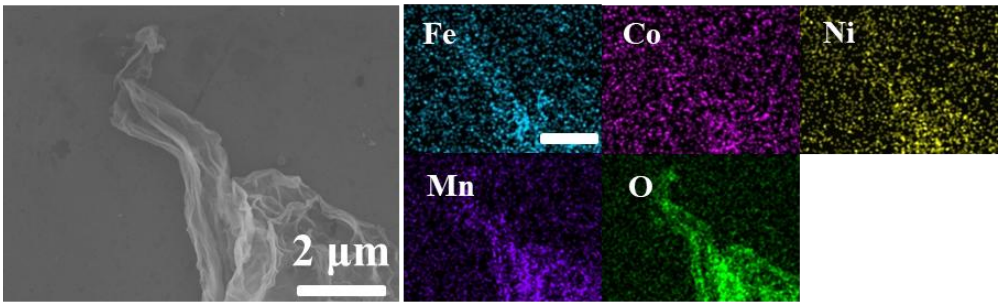

Figure S27. SEM-EDS mapping of $(FeCoNiMn)_3O_4$ after OER testing.

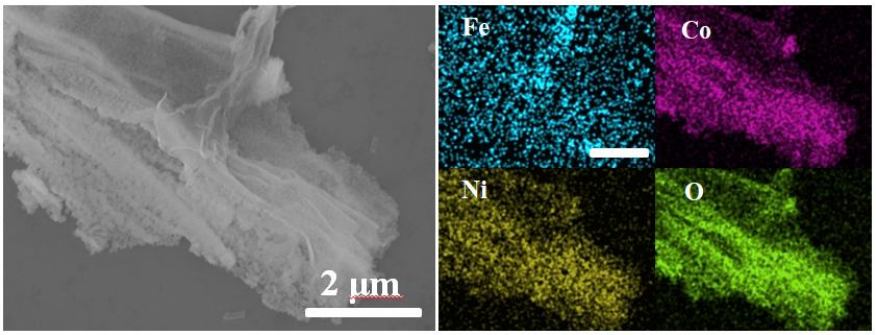

Figure S28. SEM-EDS mapping of $(FeCoNi)_3O_4$ after OER testing.

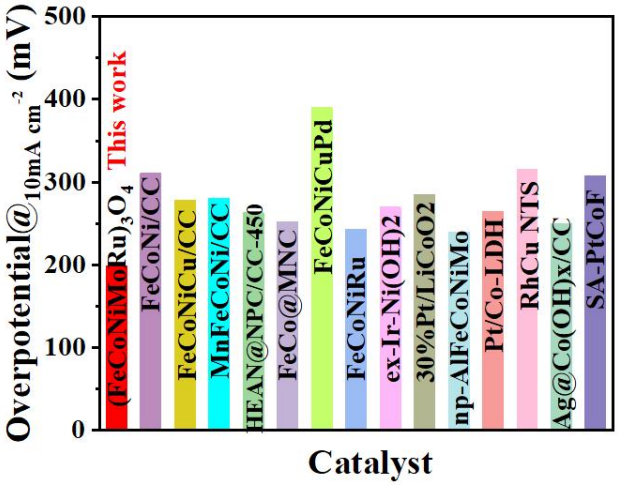

Figure S29. Comparison of OER electrocatalytic performance of our as-prepared HEOs with other reported catalysts.

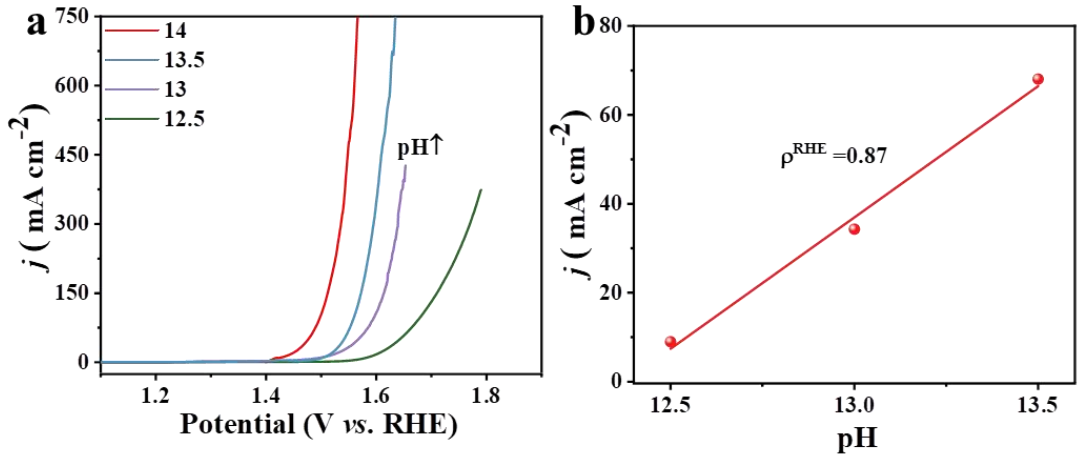

Figure S30. (a) The LSV curves of catalyst $(FeCoNiMoRu)_3O_4$ is measured in KOH electrolytes with pH = 12.5, 13, 13.5, and 14. (b) j at 1.5 V vs. RHE plotted in log scale as a function of pH, from which the proton reaction orders ($\rho^{RHE} = \partial \log (j) / \partial pH$) were derived.

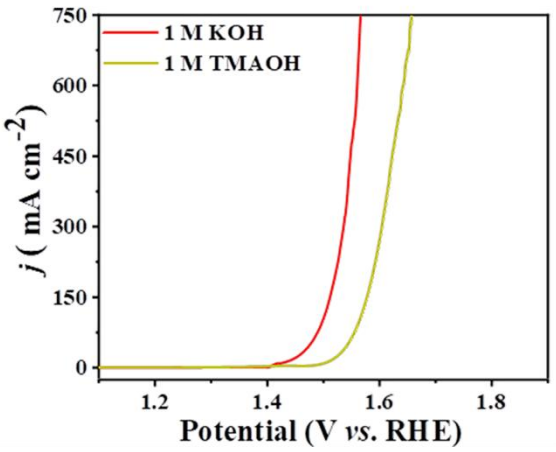

Figure S31. The LSV curves of $(FeCoNiMoRu)_3O_4$ in different solutions.

Table S1. Comparison of OER performance of $(FeCoNiMoRu)_3O_4$ and recent reported electrocatalysts at 1 M KOH electrolyte.

Catalyst	Potential (vs. RHE) (at 10 mA cm^{-2})	Tafel slope (mV dec^{-1})	References
$(FeCoNiMoRu)_3O_4$	**1.43**	**40.0**	**This work**
$(FeCoNiCrMn)_3O_4$	1.49	57.0	This work
$(FeCoNiMoMn)_3O_4$	1.59	57.2	This work
$(FeCoNiMn)_3O_4$	1.59	74.7	This work
$(FeCoNi)_3O_4$	1.62	83.8	This work
$NiFeXO_4$ (X=FeNiAlMoCoC)	1.43	53.3	ACS Nano, 2023, 17, 1485-1494
AlNiCoRuMo	1.50	54.5	ACS Mater. Lett. 2020, 2, 1698-170
RuNiMoCrFeOx/CNT	1.45	47.0	J. Mater. Chem. A, 2022, 10, 21260-21265
FeCoNiB	1.81	46.0	Small, 2019, 15, 1804212
(MgMnFeCoNi)Sn(OH)$_6$	1.53	46.8	J. Am. Chem. Soc., 2023, 145, 1924-1935
$Fe_{0.5}CoNiCuZn_{0.8}$	1.57	48.0	J. Mater. Sci. Technol., 2021, 93, 110-118
$(Cr_{0.2}Mn_{0.2}Fe_{0.2}Co_{0.2}Ni_{0.2})_3O_4$/GC	1.55	54.5	Chem. Eng. J., 2022, 431, 133448
CoNiCuMnAl@C/NF	1.45	68.8	Chem. Eng. J., 2022, 429, 132410
FeCoNiMnCu/Alloy	1.51	35.6	Chem. Eng. J., 2021, 425, 131533
Pt@LDH-4h / CC	1.49	28.4	Small, 2023, 19, 2207044.
Ni-Fe LDH hollow nanoprisms	1.51	49.4	Angew. Chem. Int. Ed., 2018, 57, 172-176.
$(FeCoNiCrMn)_3O_4$-400/CP	1.518	60	Sustain. Energy Fuels, 2022, 6, 1479
CoFeCuMoOOH@Cu/Cu foil	1.44	48.8	Adv. Mater., 2021, 22, e2100745
MnFeCoNiCu	1.49	43.0	J. Mater. Chem. A, 2020, 8, 11938-11947
FeCoNiCrMnO/HCS-3	1.49	42.2	Colloid Interface Sci., 2024, 653, 179-188.
FeCoNiMg-LDH	1.53@100 mA cm^{-2}	75.0	ACS Catalysis, 2023, 13, 7698-7706.

Table S2. Comparison of the OER performance with recently reported electrocatalysts in alkaline electrolytes.

Catalyst	Stability	Mass activity ($A\ g^{-1}$)	TOF (s^{-1})	References
$(FeCoNiMoRu)_3O_4$	**100 h @100 mA cm^{-2}**	**1281 @320 mV**	**0.23 @320 mV**	**This work**
$(FeCoNiCrMn)_3O_4$	---	112 @320 mV	0.011 @320 mV	This work
Ni_2MO_4 (M=FeCoCrMn)	92 h @10 mA cm^{-2}	267 @400 mV	0.09 @400 mV	J. Colloid Interface Sci., 2023, 646, 89-97
$Ho_2Ru_2O_7$ (HRO)	10 h @10 mA cm^{-2}	---	0.08 @300 mV	J. Mater. Chem. A, 2022, 10, 9419-9426.
HEA-5@Ir	100 h @10 mA cm^{-2}	276 @300 mV	---	SusMat., 2022, 2, 186-196